



Article

A Prototype for Computing the Distance of Features of High-Pressure Die-Cast Aluminum Products

Luis Alberto Arroniz Alcántara ^{1,2}, Óscar Hernández-Uribe ^{3,*}, Leonor Adriana Cárdenas-Robledo ⁴ and José Alejandro Fernández Ramírez ⁵

- Posgrado CIATEQ A.C., Av. del Retablo #150, Constituyentes-Fovissste, Queretaro 76150, Mexico; luis.arroniz@bocar.com
- ² AUMA (BOCAR Group), Carretera San Luis Potosí Matehuala Km 11.1, San Luis Potosi 78439, Mexico
- ³ CIATEQ A.C., Av. Manantiales #23-A, Parque Industrial Bernardo Quintana, Queretaro 76246, Mexico
- ⁴ CIATEQ A.C., Parque Industrial Tabasco Business Center, Tabasco 86693, Mexico; leonor.cardenas@ciateq.mx
- Facultad de Ingeniería, Universidad Politécnica de Tlaxcala, Av. Universidad Politécnica #1, San Pedro Xalcaltzinco, Tlaxcala 90180, Mexico; josealejandro.fernandez@uptlax.edu.mx
- * Correspondence: oscar.hernandez@ciateq.mx

Abstract: Automotive manufacturers are changing their product models faster due to the customization of users' demands. In response, suppliers must react by improving the flexibility of their means of production and making the changeover process more efficient and agile to avoid monetary losses. This article reports a prototype that uses computer vision, deep learning algorithms, and mathematical methods to derive the spatial position (x, y, z) of features of the machined parts of high-pressure die-casting (HPDC) aluminum products. It uses an RGB-D sensor to capture and process an image with the you only look once (YOLO) algorithm to determine the center of specific workpiece features. With this information, the feature depth of each center is obtained from the depth matrix and then introduced into a polynomial regression formula to acquire the spatial position (x, y, z) in millimeters. The prototype is a complementary tool for quickly sampling workpieces in the production line and verifying that they meet the requirements and specifications of spatial distances among features. With this evidence, only if necessary, the piece is sent for further and comprehensive measurement by a coordinate-measuring machine (CMM), in line with the accuracy demanded by the automotive industry.

Keywords: noninvasive measurement; deep learning; computer vision; YOLO



Academic Editors: Salik Khanal and Vitor Filipe

Received: 28 February 2025 Revised: 4 April 2025 Accepted: 7 April 2025 Published: 11 April 2025 Citation: Alcántara, L.A.A.;

Hernández-Uribe, Ó.; Cárdenas-Robledo, L.A.; Ramírez, J.A.F. A Prototype for Computing the Distance of Features of High-Pressure Die-Cast Aluminum Products. *Appl. Sci.* **2025**, *15*, 4230. https://doi.org/ 10.3390/app15084230

Copyright: © 2025 by the authors. Licensee MDPI, Basel, Switzerland. This article is an open access article distributed under the terms and conditions of the Creative Commons Attribution (CC BY) license (https://creativecommons.org/licenses/by/4.0/).

1. Introduction

The automotive industry relies on trustworthy suppliers that consistently comply with quality, time, and cost demands [1]. In the beginning stages of this industry, the lifetime of vehicle components was 20 years [2]. Currently, to comply with constant changes in user demand and the widespread introduction of electronic devices in the central functions of cars [3], manufacturers have decreased the vehicle development time and lifetime of their products, causing changes in the supply chain [4]. Hence, auto parts manufacturers produce different models of automotive pieces with complex geometries by executing short batches supported by digital transformation [5]. In this vein, coordinate-measuring machines (CMMs) are employed to guarantee the machined quality of vehicle parts from the early stages of production as a preventive way to avoid automotive recalls [6].

The CMM validates the measurement tolerances of the piece, and based on the results, the production department makes fine adjustments to or conducts the recalibration of the

Appl. Sci. 2025, 15, 4230 2 of 18

manufacturing equipment to start the production order. While CMMs are considered the benchmark in the automotive industry by being micro-precise, such machines depend on operator skills, tactile methods, or probe calibration [7]. It is worth noting that when parts change frequently or possess complex geometries, operators invest most of their time in analyzing and designing measurement strategies, reprogramming the CMM, or creating a fixture and a clamping strategy [8,9], making the process slow and expensive. In addition, the costs associated with CMM installation and maintenance are very high to prevent measurements from being affected by contamination or temperature changes [10]. Thus, such a machine is impractical for in situ quality control applications [11].

Artificial intelligence (AI) has solved industrial problems and undergone rapid growth via hardware architectures and software frameworks [12,13] that support machine learning (ML) and deep learning (DL) applications [14]. A DL architecture that has evolved quite fast is the convolutional neural network (CNN), which several models employ as a backbone [15]. In the automotive sector, AI algorithms are applied successfully in several computer vision (CV) tasks, such as the virtual construction of vehicles [16], the design of electrodes and electrolytes for vehicles' batteries [17], and electric vehicle air conditioning control [18]. Thus, AI-driven software and CV systems offer the flexibility and adaptability required by the industry (without interrupting the manufacturing process) to face constant changes due to a short development time and lifetime and the small-batch production of pieces with a diversity of materials and intricate surfaces [19,20].

The flexibility patterns required by the automotive industry make suppliers face the need to produce different types of parts in small batches, creating changes in their workflow. Manual defect detection methods suffer from low efficiency [21], and the CMM's limitations are barriers that restrict rapid adaptation to such changes. CV key tasks, such as object and feature detection, support the manufacture of any object to meet specific criteria related to quality control, measurement, and monitoring [22,23] and provide an alternative way to face several industrial challenges. For instance, Liu et al. [24], based on the fusion of an RGB and depth image, extracted the spatial position parameters of a tire and identified four features, and Cuesta et al. [25] created a ceramic artifact with a broad assortment of dimensional and geometrical tolerances (e.g., sphere, cylinder, cone) for the metrology benchmarking of four 3D-scanning sensors.

The motivation for conducting this work is related to the elapsed time (minutes or even hours) to confirm that an automotive machined workpiece is within the specified tolerances using a CMM. In this regard, the production line is inactive until approval to continue the process is received, affecting the non-productive costs per minute. Thus, this work presents a prototype to support inline verification to detect possible quality defects in machined pieces made of high-pressure die-casting (HPDC) aluminum, serving as a decision-making tool. It acts as a measurement instrument to verify whether the piece complies with the set parameters and to detect errors early that serve as evidence before sending a workpiece to the CMM laboratory. The proposed prototype uses a low-cost depth sensor and AI to locate the machined features on HPDC automotive parts. It takes advantage of CV systems' speed to compute feature distances belonging to an HPDC aluminum piece, taking a shorter time than a CMM. Thus, it reduces time, continuous movements, and stoppage on production lines.

This document is organized as follows: Section 2 presents a literature review with related works; Section 3 describes the materials and methods used in this work; Section 4 outlines the results and discussion, shows a couple of cases to measure workpiece features, and discusses the outcomes and findings; and Section 5 presents the conclusions and future work.

Appl. Sci. 2025, 15, 4230 3 of 18

2. Literature Review

The first subsection presents the evolution of you only look once (YOLO) family models and research works applying DL to solve industrial problems using RGB-D sensors. The second subsection describes related works in measuring or computing distances and geometric features in the automotive industry.

2.1. Background

Researchers seek to generate DL models with a lower computational cost and higher speed, such as Faster R-CNN [26] or YOLO [27], YOLOv3 [28], YOLOv5 [29], YOLOv7 [30], and recently, YOLOv12 [31] algorithms.

The YOLO family has been used to search for and classify objects within images. YOLOv3 delivers high precision and accuracy in detecting small objects, achieved by presenting the same image at three scales using a network called Darknet-53 [28]. However, it struggles to align the bounding boxes with the object perfectly. The YOLOv3 up to YOLOv5 algorithms have a similar architecture (moving from Darknet-53 to CSPDarknet-53), with slight changes to focus on small objects [32]. Research works report close results among them and other recent architectures [33–35], particularly when the YOLOv3 architecture is enhanced [36]. For defect detection on steel pipes, one work reports a mean average precision (mAP) value for YOLOv3 higher than that for YOLOv6 and YOLOv7 [37]. Recent versions of YOLOv8, YOLOv9, YOLOv10, and YOLOv11 introduce architectural improvements to the CSPDarknet-53 backbone, and new programmable gradient information and generalized efficient layer aggregation network components in the neck [38].

The industrial applications of image processing are often limited by hardware restrictions (e.g., the resolution, quality, and precision of the image) [39] or environmental conditions (i.e., illumination and background of the surroundings) [40], and the distance of the object and its features or defects [41]. Nevertheless, numerous applications successfully overcome these limitations, for instance, employing high-resolution cameras to locate typical defects in product manufacturing [42,43]. Regarding sensor modalities, RGB-D cameras with a limited operation range operate effectively under diverse lighting conditions [44]. The Intel RealSense sensor family includes a stereo-depth module, RGB sensor, and infrared projector, and has been widely used for prototype applications [45]. Specifically, the D400 series is employed as a fruit spatial position estimator [46] and in ergonomics [47]. Additionally, there are approaches for the segmentation of 3D objects using AI to determine what 3D objects exist in a 2D image [48] and for the digital reconstruction and visualization of 3D objects from a series of 2D images [49].

2.2. Related Works

In the automotive industry, particularly in the context of aluminum or steel products, there are alternatives to CMM that use contact metrology, as in the work of Rajamohan et al. [50], who employed a five-axis CNC machining center and a probe to measure a high-precision workpiece, where most geometric deviations were smaller than the CMM measurements. As for non-contact equipment or devices for the achievement of similar goals, several works use CV systems, DL, and ML techniques in the workpiece detection of defects or the measurement of features. Patel and Kiran [51] used linear regression, whereas Palani and Natarajan [52] implemented a self-organized artificial neural network to predict the surface roughness of pieces. Jiang et al. [53] classified X-ray images of pieces with small inter-class and large intra-class differences as defective or non-defective casting with a CNN. Similarly, Parlak and Emel [33] used YOLOv5 to classify defects as gas holes and shrinkages based on the ASTM E155 standard. Schlotterbeck et al. [54]

Appl. Sci. 2025, 15, 4230 4 of 18

performed an inline evaluation for tomography scanning to automate defect detection in alloy-casted parts.

Yi-Cheng and Syh-Shiuh [55] implemented an on-machine measurement system for the thread dimensions of a workpiece. They compared its efficiency with measurements from a 3D microscope, obtaining high-accuracy results. Pérez et al. [56] presented a 3D real-time quality inspection platform to measure automotive cast-iron parts using 3D line scan sensors. Likewise, Zou et al. [57] proposed a roughness estimation method via the line blur functions of edges reflected from machined surfaces.

Huang et al. [58] developed a target inspection method to detect, classify, and measure welding studs. They replaced the YOLOv8's backbone with an HGNetV2 network reparametrized to Rep_HGNetV2, improving small-target detection. Khow et al. [59] proposed an enhanced YOLOv8 that adds a formula to compute the ratio between the object size and the size indicated by bounding boxes. With this method, the output returns the distance of the objects detected with an accuracy of 90%. Similarly, Gasienica-Józkowy et al. [60] used YOLOv8, homography-based mapping, and polynomial regression algorithms to estimate the distance and height of objects in monocular and thermal images, achieving an accuracy of 98.86%. Huang et al. [61] employed a 3D CV system for the defect detection of an aluminum welding surface and a Gaussian planar correction algorithm to measure the area of different defects, obtaining a measurement error lower than 20%.

3. Materials and Methods

This section presents the elements of the prototype and the algorithms involved in its development, summarized in Figure 1, which illustrates the sequence followed to obtain an output matrix with the labeled spatial location for the main characteristics of an HPDC aluminum product. The subsequent subsections describe the digitizer environment functionality, the hardware and software used, and their central components. The Dataset Preparation Subsection reveals the creation and content of the files derived from the image capture. The RGB-D images taken from the sample that includes HPDC aluminum workpieces have three to four features each (e.g., cast bore, drilled bore, machined flange, screw seat). In the final subsection, the algorithm to obtain distances shows a matrix containing the data (i.e., label, spatial position). The proposal provides an inline decision-making tool for partial verification to know whether or not a piece is within the specified tolerances without using a CMM.

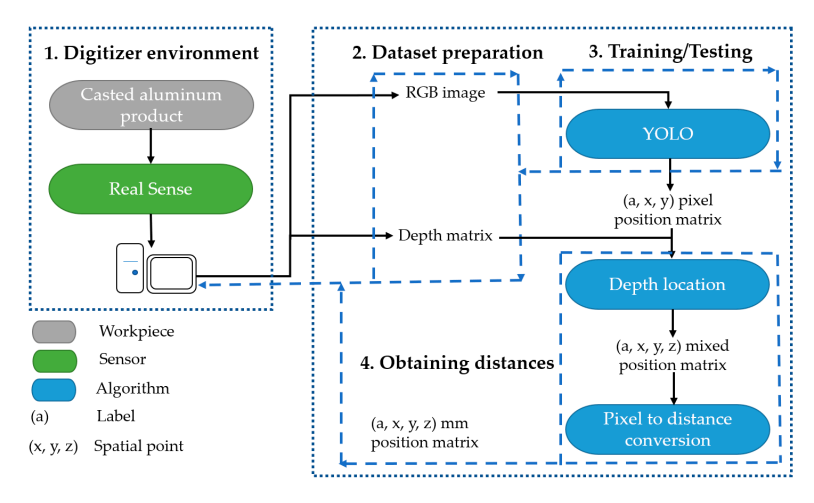
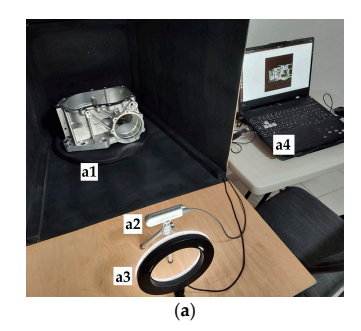


Figure 1. Flowchart of the prototype with subtasks for its deployment.

Appl. Sci. 2025, 15, 4230 5 of 18

3.1. Digitizer Environment

Figure 2a depicts the digitizer environment to avoid external environmental influence, indicating the main components with letters. It has a pyramidal frustum made of laminated wood and painted internally with matte black. The internal closed base area, measured in millimeters (mm), has a length of $400 \text{ mm} \times 400 \text{ mm}$, and the external open base has a length of $580 \text{ mm} \times 610 \text{ mm}$. The apothem lengths that join the bases are as follows: inferior—580 mm; superior—600 mm; and lateral—610 mm. A circular rotative plate (a1) spins the piece, and the captured position images are obtained by an Intel RealSense D415 camera (a2) with an LED ring illumination source (a3). The camera captures a 2D mesh for the color image (RGB) and a matrix with the depths of each pixel, known as a depth matrix. It has a depth range of 300 mm–3000 mm and a resolution of 1 mm.



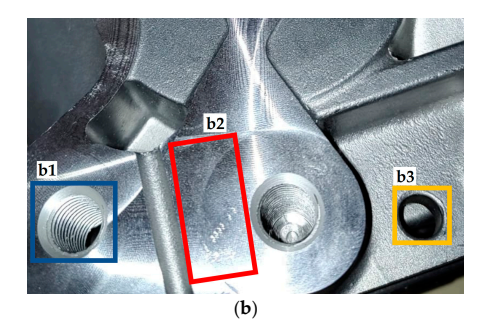


Figure 2. The prototype setup: (a) digitizer environment; (b) features of a machined workpiece.

The prototype employs an Asus gaming laptop with an Intel Core I5 processor, an Nvidia GeForce video card, an Ubuntu 22.04.2 LTS operating system, and the Python programming language (a4). On the other hand, the HPDC aluminum parts present different geometrical shapes with several cast bores, which are CNC-machined for a posterior component assembly. Figure 2b depicts the features of a machined workpiece, such as formed threads (b1), the machined flange (b2), and the cast bore (b3).

3.2. Dataset Preparation

The authors have created a database with images of HPDC aluminum parts based on the workflow depicted in Figure 3. First, the user initializes and configures the RealSense camera to obtain an RGB-D image with a pixel resolution of 640×480 and places a casted part on the rotative plate. Next, a data frame stores the information, structured as [[R, G, B, D], [pixel 2], . . . , [pixel n]]. Then, this data frame is trimmed of its outer parts, reducing its dimensions to 448×448 pixels without sacrificing resolution, and three files in CSV format save the data: one contains image information, the other the corresponding configuration of the bounding boxes, and the last the correlation between them. The circular plate rotates a few degrees, restarting the sequence to capture enough images of each casted workpiece. As part of the preprocessing and cleaning task, the user identifies the adequate bounding boxes of each image and labels every feature. Finally, the above files serve as a dataset to train the YOLOv3 and YOLOv11 algorithms.

Figure 4 displays the workflow to identify labels and bounding boxes. The user selects the image to be analyzed and scales it to identify the features, picking a box that better fits the feature, pressing the enter key to accept the selection, and repeating these actions with a different feature.

Appl. Sci. 2025, 15, 4230 6 of 18

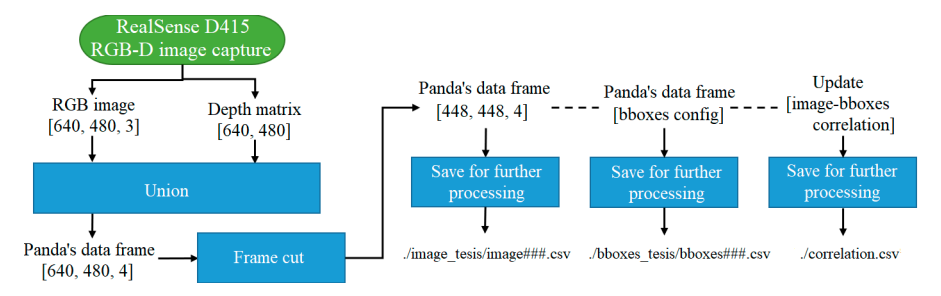


Figure 3. Image capture and dataset processing workflow (# indicates the image number with the corresponding bounding box data).

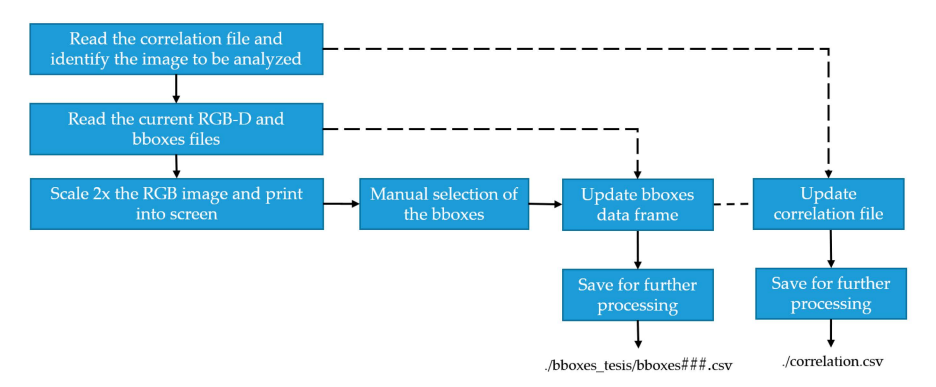


Figure 4. Workflow for manual identification of labels and bounding boxes (# indicates corresponding bounding box data).

Figure 5 depicts an example of a workpiece with the features' locations after the user locates the features in the piece identified by bounding boxes. The user interface presents five tags for each bounding box: label, x_center, y_center, width, and height. The label represents a number between 0 and 3 that identifies the feature; x_center and y_center define the geometrical center; and width and height limit the rectangle's dimensions. The dataset contains 360 images corresponding to 20 workpieces captured in different positions. The resulting image data captured for each piece are normalized to recover the data with the bounding boxes at every scale.

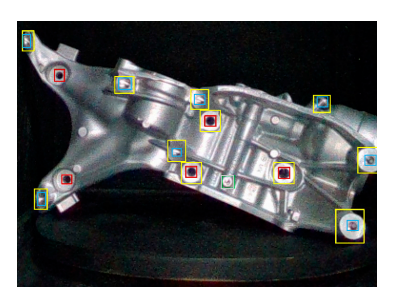


Figure 5. Location of features identified by bounding boxes: cast bore (red), screw seat (yellow), and drilled bore (blue).

3.3. Training and Testing

The YOLO algorithms utilize 1000 images corresponding to 20 different workpieces (e.g., housing, bracket, or cover) with three to four features each. The proposal uses data augmentation (i.e., translation, rotation, and horizontal and vertical flip) to reach 50 images for each workpiece. Figure 6 presents the workflow for the training process, and a CSV file stores the information at the end. The algorithms apply three prediction blocks (e.g., big, medium, and small objects) as inputs of a max pool layer that predicts the label of the feature, the center point of the feature (x, y), and the width and height of the bounding box. For YOLOv3 and YOLOv11, the parameters used in the proposed prototype are a batch

Appl. Sci. 2025, 15, 4230 7 of 18

size of 4, image size of 448, number of features of 4, and learning rate of 1×10^{-4} . Since the prototype is employed in Mexico, Table 1 shows a Spanish to English translation.

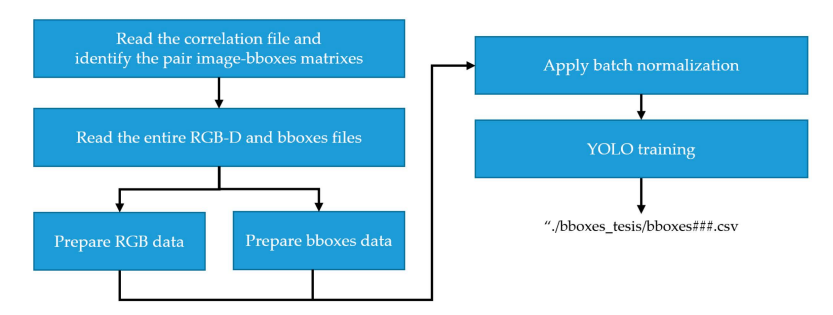


Figure 6. YOLOv3 and YOLOv11 training workflow (# indicates related bounding box data).

Table 1. Features and labels used in prototype.

Feature in Spanish	Feature in English
Barreno de fundición	Cast bore
Barreno maquinado	Drilled bore
Brida maquinada	Machined flange
Asiento de tornillo	Screw seat

3.4. Obtaining Distances

The model outputs feed a polynomial algorithm, observed in Equation (1), that converts pixels into mm using the depth matrix. Figure 7a depicts an aluminum 3D-printed pattern to obtain the indexes by placing it in front of the sensor at 40 different distances. Each iteration builds a matrix and considers a cross-section to locate the initial and final point of the pattern, representing the piece in 200 mm and computing its value in pixels—the distance ratio results from the points at a given depth by dividing them by 200 mm. Figure 7b shows the resulting polynomial behavior.

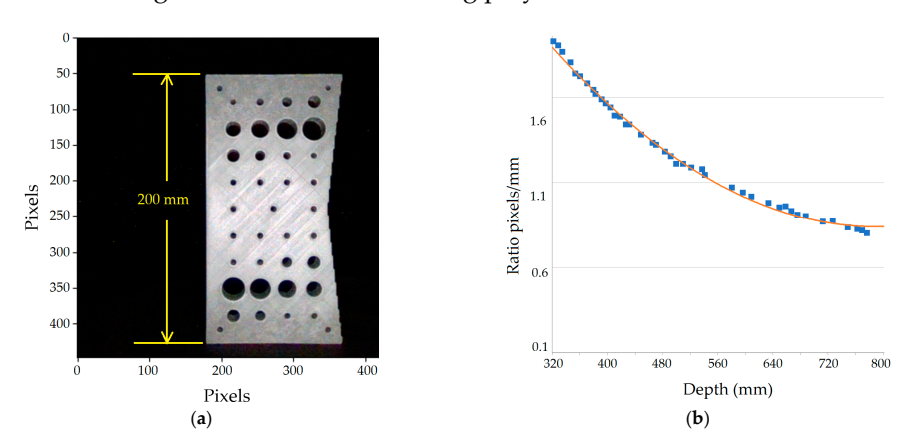


Figure 7. Adjustment to obtain ratio of pixels to mm: (a) 3D pattern used to obtain the polynomial indexes; (b) resulting polynomial curve.

Finally, the least square method was applied using Equation (2), and the point represented by [x_center, y_center] in pixels is located in the distance matrix to obtain the spatial location and depth in mm. In a workpiece, given two drilled bore centers measured in pixels, for the first, P0(x, y) = (321, 754) as the origin point, and for the second, P1(x, y) = (318, 435); using Equation (2) results in P0(x, y) = (109.151547, 525.7794206) and a depth of 493 mm, and P1(x, y) = (108.250914, 214.2178846) with a depth of 482 mm.

$$y = a_0 + a_1 x_i + a_2 x_i^2 + a_3 x_i^3 + \ldots + a_m x_i^m + \epsilon_i$$
 (1)

Appl. Sci. 2025, 15, 4230 8 of 18

$$\begin{bmatrix} 3.063809041 - 6.292055889x_{pixels} + 4.168540127x_{pixels}^{2} \\ 2.701041432 - 5.547050558y_{pixels} + 3.674967808y_{pixels}^{2} \end{bmatrix} = \begin{bmatrix} x_{mm} \\ y_{mm} \\ z_{mm} \end{bmatrix}$$
(2)

Furthermore, the Pythagoras theorem is employed to find the relative distance between P0 and P1 with a value of 239.0 mm. Therefore, to calculate the relative distances for any piece, the point on the *x*-axis and *y*-axis that belongs to the feature closest to the center point of the image was selected as the origin of the piece.

4. Results and Discussion

This section presents the following: 1. the results of YOLOv3 and YOLOv11 training, validation, and testing with the dataset created; 2. the spatial distances computed by the program for three HPDC aluminum workpieces; 3. an on-site test to compare the specified distances for each piece against the measurements obtained with the prototype; and 4. a discussion section highlighting the models employed.

4.1. Training, Validation, and Testing

The YOLO algorithms used 1000 images corresponding to 20 pieces, divided into validation, training, and testing sets. The training set comprises 700 images, 35 for each piece. Of the images, 150 correspond to the validation set and 150 to the test set; each piece has 15 images. The training and validation loss curve converges at epoch 200, whereas the mAP curve reaches its best behavior at epoch 240 (YOLOv3) and 220 (YOLOv11). In the mentioned epochs, feature selection and object detection have accuracies above 90% for both algorithms. In addition, the model YOLOv3 employed four learning rate values— $lr = 1 \times 10^{-3}$, $lr = 5 \times 10^{-4}$, $lr = 1 \times 10^{-4}$, and $lr = 5 \times 10^{-5}$ —to evaluate the network's performance according to the above metrics. It is worth noting that YOLOv3 presents better results with an $lr = 1 \times 10^{-4}$. Therefore, for YOLOv11, the lr used is lr 10⁻⁴, obtaining better results than YOLOv3. Figure 8 illustrates the performance graphs with validation sampled every ten epochs. Figure 8a shows the loss behavior, which is better when it is closer to 0. YOLOv3 obtains a value of 1.51 and YOLOv11 a value of 0.78.

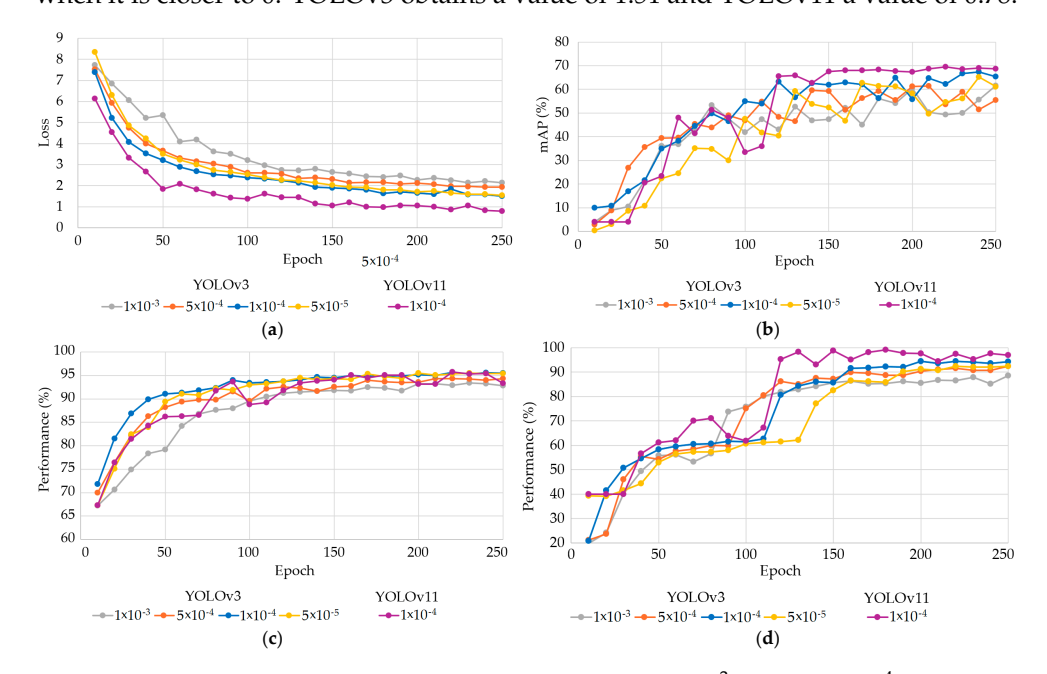


Figure 8. Validation metrics for different learning rate values (1×10^{-3}) is gray, 5×10^{-4} is orange, 1×10^{-4} is blue, and 5×10^{-5} is yellow for YOLOv3; and 1×10^{-4} is purple for YOLOv11): (a) loss performance; (b) mAP performance; (c) feature selection accuracy performance; (d) object selection accuracy.

Appl. Sci. 2025, 15, 4230 9 of 18

Figure 8b depicts the mAP behavior; the best value is that closest to 100%. YOLOv3 achieves a value of 67%, whereas that of YOLOv11 is 69%. Figure 8c indicates how accurate the algorithm is in identifying features; YOLOv3 attains a value of 95%, whereas that of YOLOv11 is 96%. Figure 8d presents the behavior for object detection, where YOLOv3 reaches a performance of 95%, and YOLOv11 delivers a value of 98%. Table 2 summarizes the performance of the four indicators for each YOLO algorithm, assuming an $lr = 1 \times 10^{-4}$ for both versions, with the best performance at epoch 247 for YOLOv3 and 243 for YOLOv11. Both algorithms locate the features of the HPDC aluminum part. As mentioned, the user interface includes a section that presents some images from the validation dataset, with the prediction outcome, their bounding boxes, and labels (useful for manual validation). Figure 9 illustrates two analyzed images, the bracket and housing pieces, and features (i.e., drilled bore, screw seat, and machined flange), identifying them appropriately with their closest centers.

Table 2. Summary of validation performance	Table 2.	Summary	of validation	performance.
---	----------	---------	---------------	--------------

Model Description		Loss	mAP	Feature Selection	Object Selection
YOLOv3	Value (best epoch)	1.44 (247)	0.652 (240)	95.91% (246)	94.62% (203)
	Average for last 50 data points	1.58	0.575	95.32%	93.67%
YOLOv11	Value (best epoch)	1.02 (243)	0.613 (203)	97.54% (220)	97.69% (240)
	Average for last 50 data points	1.16	0.628	87.62%	96.22%

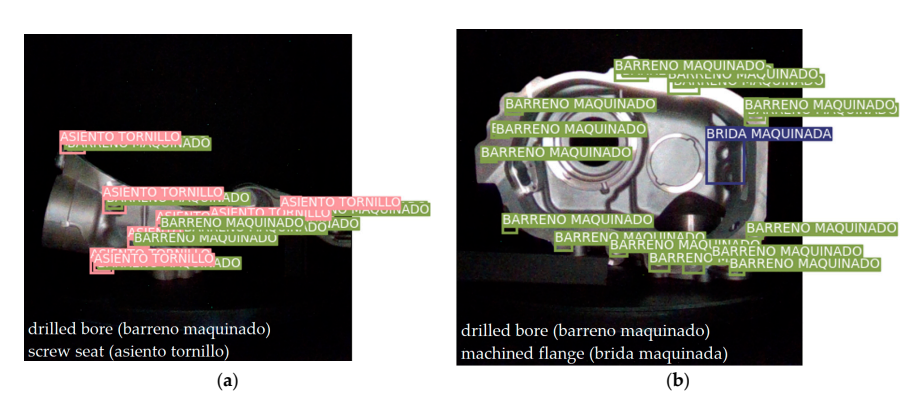


Figure 9. Two examples of analyzed images: (a) a bracket; (b) a housing.

4.2. Spatial Distances

This section presents the results and analysis of using YOLOv3 with three HPDC aluminum workpieces: a housing, bracket, and cover. Each piece includes a figure illustrating the sequence of image processing and two tables: one with a summary of the detected features (e.g., cast bore, drilled bore, machined flange, and screw seat) and another with a particular feature (drilled bore) positions in pixels and mm for comparison with the specified measurements, the columns x and y represent the center of a feature, and x, y, and z are the corresponding values in mm. Extra columns show the calculated distance, the specified distance by design, and the absolute error. The first row represents the center of the feature considered as the base to compute the distances in the subsequent rows.

Housing. The frontal image of the housing shows eight different drilled bores (8 mm), two screw seats (10 mm), and one casted bore (10 mm). Figure 10 depicts the workpiece on the circular plate, the detected features, and the depth image. Table 3 summarizes the number of features found in the current workpiece. For this piece, the prototype's detection accuracy reaches an average of 75.0%. Table 4 presents the results for each drilled bore's calculated distance (Calculated D) compared to the distance specified by design (Specified

D). It describes six drilled bores, with an average error of 0.219 mm and a maximum error of 0.277 mm for a distance of 150.5 mm, representing a 0.18% error.

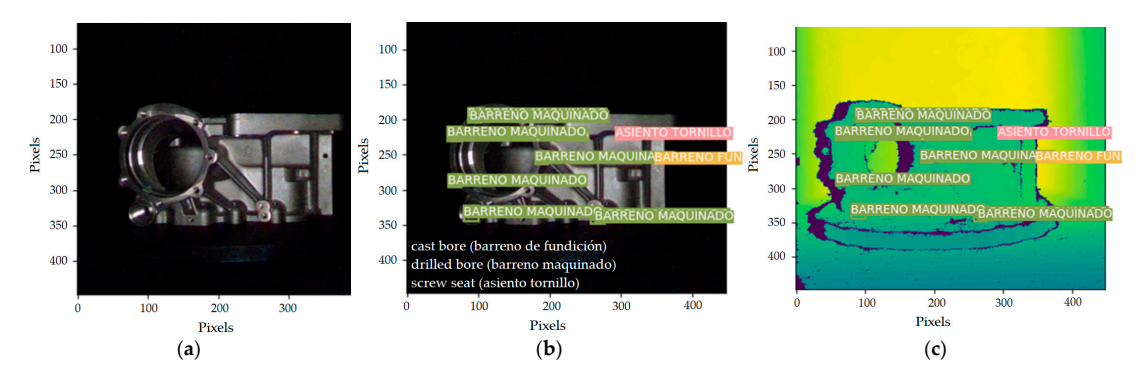


Figure 10. Sequence of image processing for the housing: (a) original image; (b) RGB-analyzed image; (c) depth-processed image.

Table 3. Summary of detected characteristics for the housing.

Feature	Quantity	Detected	Accuracy
Cast Bore	1	1	100.0%
Drilled Bore	8	6	75.0%
Screw Seat	2	1	50.0%

Table 4. Detected centers of drilled bores and relative distance to the first point (housing).

x Pix	y cels	x	y mm	z	Calculated D mm	Specified D mm	Error mm
188	253	-44	31	459	0.000	0.000	0.000
267	337	50	116	475	127.738	128.000	0.262
66	286	-188	65	466	148.125	148.000	0.125
66	207	-186	-18	472	150.777	150.500	0.277
89	333	-159	113	472	141.838	142.000	0.162
94	193	-155	-33	465	128.269	128.00	0.269

Bracket. The frontal image of the bracket displays seven drilled bores (8 mm), seven screw seats (10 mm), and five casted bores (10 mm). Figure 11 depicts the workpiece on the prototype, the detected features, and the depth image. Table 5 presents the number of features of the workpiece. In this case, the prototype's detection accuracy reaches an average of 80.0%. Table 6 shows the results for the drilled bores' distances compared to the specified distances. It describes seven drilled bores, with an average error of 0.133 mm and a maximum error of 0.233 mm for a distance of 56.5 mm, representing a 0.41% error.

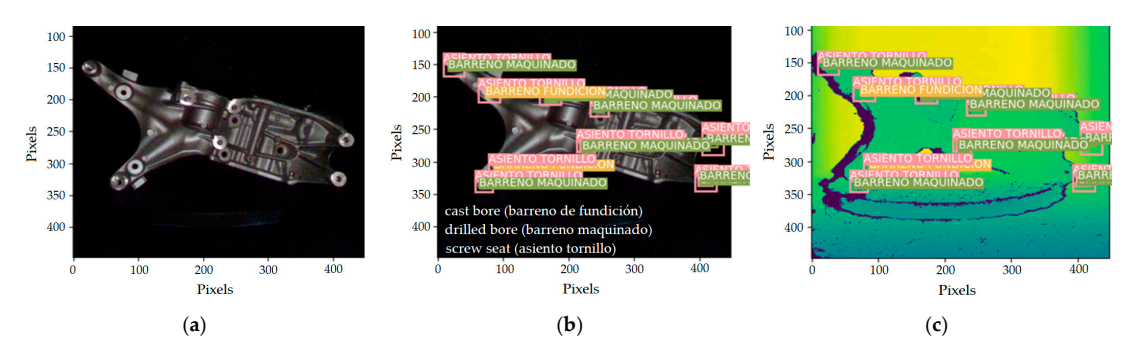


Figure 11. Sequence of image processing for the bracket: (a) original image, (b) RGB-analyzed image, (c) depth-processed image.

Table 5. Summary of detected characteristics for the bracket.

Feature	Quantity	Detected	Accuracy
Cast Bore	5	2	40.0%
Drilled Bore	7	7	100.0%
Screw Seat	7	7	100.0%

Table 6. Detected centers of drilled bores and relative distance to the first point (bracket).

x Pix	y xels	X	y mm	z	Calculated D mm	Specified D mm	Error mm
225	268	1	42	515	0.000	0.000	0.000
246	214	23	-9	524	56.267	56.500	0.233
409	325	189	91	541	196.021	196.000	0.021
419	267	191	37	560	195.320	195.500	0.180
24	151	-232	-75	479	263.199	263.000	0.199
70	332	-173	107	494	186.928	187.000	0.072
173	198	-59	-27	480	97.908	98.000	0.092

Cover. This workpiece was new to the model (not seen before). The frontal image depicts three machined flanges (12 mm), twelve drilled bores (6 mm), six screw seats (8 mm), and three casted bores. Figure 12 illustrates the workpiece on the circular plate, the detected features, and the depth image. Table 7 indicates the number of features of the workpiece. The prototype's detection accuracy reaches an average of 81.2% for the cover piece. Table 8 exhibits the results for the drilled bores' distances compared to the specified distances. It describes eleven drilled bores, with an average error of 0.123 mm and a maximum error of 0.27 mm for a distance of 113.0 mm, representing a 0.24% error.

Table 7. Summary of detected characteristics for the cover.

Feature	Quantity	Detected	Accuracy
Cast bore	3	3	100.0%
Drilled bore	12	11	91.7%
Machined flange	3	1	33.3%
Screw seat	6	6	100.0%

Table 8. Detected centers of drilled bores and relative distance to the first point (cover).

x	y ixels	x	y mm	z	Calculated D mm	Specified D mm	Error mm
246	357	37	198	303	0.000	0.000	0.000
		-					
272	386	74	221	344	59.825	60.000	0.175
290	315	113	137	299	97.535	97.500	0.035
314	355	150	193	309	113.270	113.000	0.270
424	254	320	42	557	324.193	324.000	0.193
345	137	201	-217	312	364.146	364.000	0.146
349	21	209	-298	309	525.010	525.000	0.010
352	261	217	55	302	229.891	230.000	0.109
148	70	-127	-227	307	455.562	455.500	0.062
102	348	-216	193	282	253.919	254.000	0.081
120	180	-177	-66	301	339.847	340.000	0.153

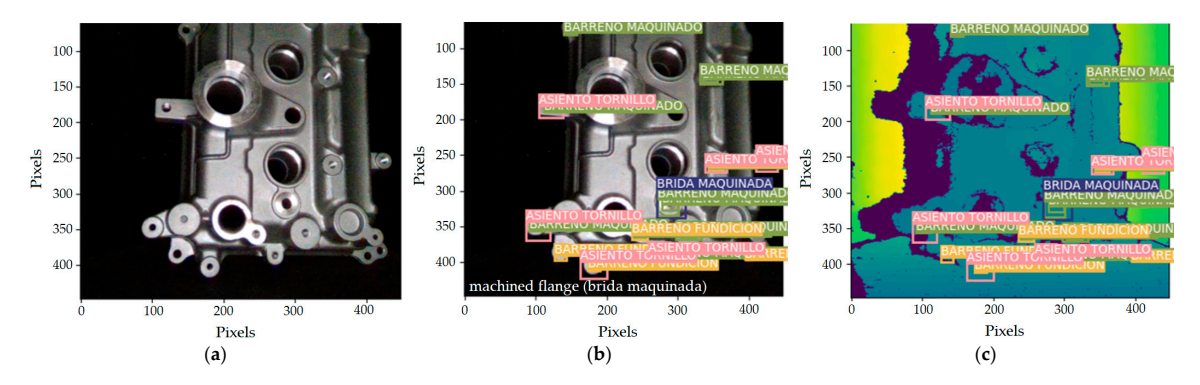


Figure 12. Sequence of image processing for the cover: (a) original image; (b) RGB-analyzed image; (c) depth-processed image.

4.3. On-Site Test with the Prototype

An automotive parts manufacturing plant served as the setting to test the prototype in a machining process line, including 17 CNC machines, two industrial washers, and 33 assembly stations. The production line manufactures two types of cylinder head covers used for vehicles, and the workpiece quality must be verified by sampling every 4 h at the final CNC operation. A worker randomly picks six CNC machines and takes the finished pieces, cleaning and tempering the sample of each machine, which takes 40 min. Following this, the operator sends the samples for measurement to the CMM laboratory. The laboratory has two CMMs available for testing purposes. Each machine measures one piece in 56 min, working for 2 h and 48 min. The remaining time is 1 h and 12 min for the operator to confirm the results and perform either the calibration or preventive maintenance of the CMM before the subsequent sampling. Figure 13 presents on-site tests conducted at the manufacturing plant, using a workpiece not employed previously by the YOLO algorithms, known as a cylinder head cover.

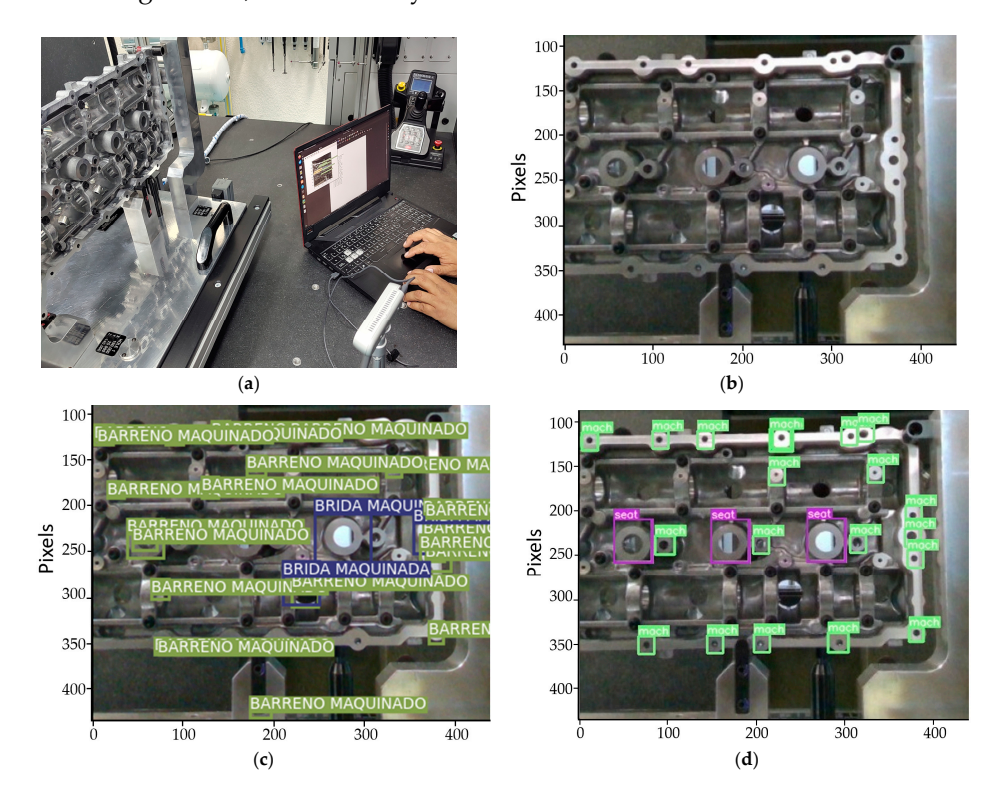


Figure 13. On-site test, a piece not used in the training or validation phase: (a) prototype installed close to the production area; (b) original image of the piece; (c) YOLOv3-analyzed image of a drilled bore (green); (d) YOLOv11-analyzed image of a drilled bore (green).

Figure 13a shows a piece not previously seen by the model and clamped on a bench in front of the RGB-D sensor in the production area. Figure 13b depicts the original image captured by the sensor. Figures 13c and 13d present the features detected using YOLOv3 and YOLOv11, respectively.

Both measurement processes are executed five times with a single piece (taking 2 min with the prototype and 25 min with the CMM each time). The process includes preparation, the identification of features, the computation of distances, analysis, and the average computation. Table 9 displays the number of features and their accuracy for the drilled bores using YOLOv3 and YOLOv11. Tables 10 and 11 present the spatial position of drilled bore features with the distance specified and the average values calculated by the prototype and obtained with the CMM. Table 10 presents the results of YOLOv3 with an average error of feature detection by the prototype equal to 0.128 mm, and the maximum error is 0.24 mm, representing 0.15%. Likewise, Table 11 delivers the outcomes of YOLOv11 with an average error of 0.183 mm, and the maximum error is 0.296 mm, representing 0.17%. It is worth mentioning the constraints specified for measurement validation: the piece is reincorporated into the production process only when the absolute error of the analyzed feature between the columns Specified D and Calculated D is lower than 0.3 mm. Indeed, such an error should represent less than 0.30% regarding Specified D.

Table 9. Summary of the detected characteristics of cylinder head covers used for vehicles.

Feature	Quantity	Detected	Accuracy
Drilled bore: YOLOv3	21	17	80.9%
Drilled bore: YOLOv11	21	19	90.5%

Table 10. Detected centers of the drilled bore and the relative distance to the first point (YOLOv3).

x Pix	y	х	y mm	z	Calculated D mm	Specified D mm	Error mm	CMM mm
246	357	37	198	508	0.000	0.000	0.000	0.000
11	122	-229	-97	515	251.970	252.000	0.030	251.866
25	182	-205	-38	536	221.172	221.000	0.172	220.884
378	251	-168	26	508	164.760	165.000	0.240	164.889
58	235	-184	11	501	192.172	192.000	0.172	191.787
76	353	-161	123	511	213.675	213.500	0.175	213.384
74	290	-157	61	530	179.666	179.500	0.166	179.384
90	123	-148	-98	504	178.779	179.000	0.221	179.014
129	180	-97	-40	541	113.428	113.500	0.072	113.616
141	117	-92	-104	502	137.339	137.500	0.161	137.622
185	419	-42	186	512	201.102	201.000	0.102	200.893
180	156	-45	-61	538	79.423	79.500	0.077	79.643
234	292	11	63	527	74.572	74.500	0.072	74.361
332	157	112	-61	534	120.021	120.000	0.021	120.111
374	204	160	-19	518	153.652	153.500	0.152	153.489
374	228	161	4	517	154.810	155.000	0.190	155.012
379	337	184	119	471	290.026	290.000	0.026	289.879

Table 11. Detected centers of the drilled bore and the relative distance to the first point (YOLOv11).

x Pix	y els	х	y mm	z	Calculated D mm	Specified D Mm	Error mm	CMM mm
246	357	37	198	508	0.000	0.000	0	0.000
11	124	-230	-95	513	252.046	252.000	0.046	251.866
25	183	-205	-37	536	220.924	221.000	0.076	220.884
378	252	-168	27	508	164.889	165.000	0.111	164.889
58	243	-184	19	501	192.265	192.000	0.265	191.787

Table 11. Cont.

x Pix	x y Pixels		y mm	z	Calculated D mm	Specified D Mm	Error mm	CMM mm
75	351	-162	121	511	213.738	213.500	0.238	213.384
74	289	-156	60	530	179.597	179.500	0.097	179.384
91	122	-146	-99	504	178.704	179.000	0.296	179.014
129	180	-97	-40	541	113.265	113.500	0.235	113.616
141	116	-92	-105	502	137.766	137.500	0.266	137.622
186	419	-41	186	512	200.795	201.000	0.205	200.893
179	157	-46	-61	538	79.753	79.500	0.253	79.643
235	292	12	63	527	74.673	74.500	0.173	74.361
333	158	113	-60	534	120.226	120.000	0.226	120.111
374	204	160	-19	518	153.723	153.500	0.223	153.489
374	228	161	4	51 <i>7</i>	154.709	155.000	0.291	155.012
334	420	118	185	518	210.623	210.500	0.123	210.672
323	405	106	170	519	191.044	191.000	0.044	190.994
379	337	184	119	471	289.879	290.000	0.121	289.879

4.4. Discussion

The prototype supports operators' decision-making to ensure that workpiece production meets quality standards by verifying that the absolute error is in range. Otherwise, the piece is sent to and measured by the CMM, optimizing this resource. In this sense, the prototype works as an in situ verification support tool, for a preliminary sampling quality assessment of manufactured workpieces. Due to the nature of the piece (i.e., morphology and restrictions), a CMM RENISHAW AGILITY s12129 is used to obtain the measurements of each feature and compute the average of five measurements as a reference to validate the prototype. In this work, the metrics employed are mean absolute percentage error (MAPE) and accuracy [62]. For the CMM, the average values were a MAPE of 0.0180%, an accuracy of 99.9820%, and a standard deviation of 0.0003 mm. For the prototype using YOLOv3, MAPE was 0.1781%, accuracy was 99.8219, and the standard deviation was 0.2578 mm. Moreover, with the use of YOLOv11, MAPE was 0.1257%, accuracy was 99.8444%, and standard deviation was 0.1989 mm. In addition, the accuracy of the feature detected (drilled bore) in off-site tests had a mean of 88.9%, whereas the on-site tests reached 80.9% for YOLOv3 and 90.5% for YOLOv11, both promising values.

This work used the YOLO architecture to detect a few workpiece features. The user iteratively identifies adequate bounding boxes to tailor the dataset to the use case to ensure the model's training on relevant features. On the other hand, the literature has reported that YOLOv3 obtained better average precision and mAP values than YOLOv4 in detecting internal defects in aluminum alloy welds [63]. Another example is the work developed by Shao et al. [64], who used a custom-designed dataset tailored to specific fire and smoke detection. They executed several YOLO models and reported that YOLOv3 scored better than YOLOv10 for fire detection and YOLOv7 for smoke detection according to their mAP values. However, the authors acknowledge that replacing YOLO with newer architectures in the fast-evolving object detection field could offer further improvements in accuracy and speed. The results reported in the above subsections demonstrate that the mAP values of YOLOv11 are slightly better than those of YOLOv3.

5. Conclusions

The presented approach provides an insightful perspective on the noninvasive measurement of HPDC aluminum products. It is relevant as a low-cost solution for small and medium enterprises that cannot afford investment in CMM or 3D scanner devices. The designed prototype contributes to applied science and industrial practice in the

Appl. Sci. 2025, 15, 4230 15 of 18

implementation of a workflow for spatial location, enabling the identification of the characteristics of interest of an aluminum workpiece. The design and implementation of the prototype involve the computation of the distance between an origin point and features of HPDC aluminum parts for the automotive industry, using YOLOv3 and YOLOv11 algorithms with different workpieces for training, validation, and testing. The prototype can locate such features using pictures taken with an RGB-D sensor.

One of the benefits of the on-site prototype is the employment of the feature detection of the workpiece using a DL method and the computation of the distances based on a polynomial approach supported by an RGB-D sensor. It allows the identification of the same features in other pieces with different shapes and complexities. The prototype works as a complementary tool for quickly sampling workpieces in a production line and verifying that they meet the requirements and specifications for spatial distances among features. Thus, only when the piece exceeds the limit values is it sent for further and comprehensive measurement at the CMM laboratory, saving time and resources. The results were promising due to the accurate feature identification achieved through immediate computations, which foster prompt decision-making. This is critical for greater flexibility in manufacturing automotive parts in response to new demands, requirements, and needs, mainly in non-repetitive production, where subsequent pieces may differ slightly.

Future work should include enhancements to the prototype, given that not all features are detected, such as the adjustment of the prototype design. For instance, changes in the size of the structure and plate would enable the measurement of pieces of a bigger size. Also, researchers should consider tuning environmental conditions (e.g., lighting quality) to work with the same settings for sampling images and commissioning. Regarding YOLO algorithms, replacing such models with newer architectures and increasing the training dataset's size to enhance feature detection should be considered. In addition, it is essential to provide the exact location of the bounding boxes by applying accurate manual identification methods. In the pixel-to-mm conversion stage, an improvement could be adding an automated metric extraction method of the features to measure the perimeter and locate its center accurately. Further tests are necessary using an RGB-D system with a micrometer scale to reach the measurement accuracy of a CMM.

Author Contributions: Conceptualization, L.A.A.A. and Ó.H.-U.; methodology, all authors; software, L.A.A.A.; validation, L.A.A.A., Ó.H.-U. and L.A.C.-R.; investigation, all authors; data curation, L.A.A.A.; writing—original draft preparation, L.A.A.A. and Ó.H.-U.; writing—review and editing, L.A.A.A., Ó.H.-U. and L.A.C.-R.; visualization, L.A.A.A., Ó.H.-U. and J.A.F.R.; supervision, Ó.H.-U. and L.A.C.-R. All authors have read and agreed to the published version of the manuscript.

Funding: This research received no external funding.

Data Availability Statement: The data presented in this study are available on request from the corresponding author.

Acknowledgments: The aluminum casted parts used for the development of this prototype were provided by Bocar Group S.A. de C.V. Thanks to the Secretaría de Ciencia, Humanidades, Tecnología e Innovación (SECIHTI) for Ph.D. scholarship support under the number CVU 771170 and SECIHTI SNI.

Conflicts of Interest: Author Luis Alberto Arroniz Alcántara was employed by the company AUMA (BOCAR Group). The remaining authors declare that the research was conducted in the absence of any commercial or financial relationships that could be construed as a potential conflict of interest.

References

1. Börold, A.; Teucke, M.; Rust, J.; Freitag, M. Recognition of car parts in automotive supply chains by combining synthetically generated training data with classical and deep learning based image processing. *Procedia CIRP* **2020**, *93*, 377–382. [CrossRef]

- 2. Paskert, L. Additive Manufacturing for the Spare Part Management of Classic Cars. Master Thesis, Stellenbosch University, Sudáfrica, South Africa, 2022.
- 3. Boissie, K.; Addouche, S.-A.; Baron, C.; Zolghadri, M. Obsolescence management practices overview in automotive industry. *IFAC-PapersOnLine* **2022**, *55*, 52–58. [CrossRef]
- 4. Zamazal, K.; Denger, A. Product lifecycle management in automotive industry. In *Systems Engineering for Automotive Powertrain Development*; Hick, H., Küpper, K., Sorger, H., Eds.; Springer: Cham, Switzerland, 2021; pp. 443–469. [CrossRef]
- 5. Rosa, E.S.; Godina, R.; Rodrigues, E.M.G.; Matias, J.C.O. An industry 4.0 conceptual model proposal for cable harness testing equipment industry. *Procedia Comput. Sci.* **2022**, 200, 1392–1401. [CrossRef]
- 6. AIAG. *Potential Failure Mode and Effects Analysis FMEA Reference Manual*, 4th ed.; Automotive Industry Action Group: Southfield, MI, USA, 2008.
- 7. Kugunavar, S.; Iyer, S.V.; Sangwan, K.S.; Bera, T.C. Data-driven model for CMM probe calibration to enhance efficiency and eustainability. *Procedia CIRP* **2024**, *122*, 885–890. [CrossRef]
- 8. Luque-Morales, R.A.; Hernandez-Uribe, O.; Mora-Alvarez, Z.A.; Cardenas-Robledo, L.A. Ontology development for knowledge representation of a metrology lab. *Eng. Technol. Appl. Sci. Res.* **2023**, *13*, 12348–12353. [CrossRef]
- 9. Kiraci, E.; Palit, A.; Attridge, A.; Williams, M.A. The effect of clamping sequence on dimensional variability of a manufactured automotive sheet metal sub-assembly. *Int. J. Prod. Res.* **2023**, *61*, 8547–8559. [CrossRef]
- 10. Thalmann, R.; Meli, F.; Küng, A. State of the art of tactile micro coordinate metrology. Appl. Sci. 2016, 6, 150. [CrossRef]
- 11. Kalajahi, E.G.; Mahboubkhah, M.; Barari, A. On detailed deviation zone evaluation of scanned surfaces for automatic detection of defected regions. *Measurement* **2023**, 221, 113462. [CrossRef]
- 12. Dhilleswararao, P.; Boppu, S.; Manikandan, M.S.; Cenkeramaddi, L.R. Efficient hardware architectures for accelerating deep neural networks: Survey. *IEEE Access* **2022**, *10*, 131788–131828. [CrossRef]
- 13. Adewumi, T.; Liwicki, F.; Liwicki, M. State-of-the-art in open-domain conversational ai: A survey. *Information* **2022**, *13*, 298. [CrossRef]
- 14. Sharifani, K.; Amini, M. Machine learning and deep learning: A review of methods and applications. *World Inf. Technol. Eng. J.* **2023**, *10*, 3897–3904.
- 15. Bhatt, D.; Patel, C.; Talsania, H.; Patel, J.; Vaghela, R.; Pandya, S.; Modi, K.; Ghayvat, H. CNN variants for computer vision: History, architecture, application, challenges and future scope. *Electronics* **2021**, *10*, 2470. [CrossRef]
- 16. Ding, Y.; Luo, X. A virtual construction vehicles and workers dataset with three-dimensional annotations. *Eng. Appl. Artif. Intell.* **2024**, 133, 107964. [CrossRef]
- 17. Sui, C.; Jiang, Z.; Higueros, G.; Carlson, D.; Hsu, P.-C. Designing electrodes and electrolytes for batteries by leveraging deep learning. *Nano Res. Energy* **2024**, *3*, e9120102. [CrossRef]
- 18. He, L.; Li, P.; Zhang, Y.; Jing, H.; Gu, Z. Intelligent control of electric vehicle air conditioning system based on deep reinforcement learning. *Appl. Therm. Eng.* **2024**, 245, 122817. [CrossRef]
- 19. Islam, M.R.; Zamil, M.Z.H.; Rayed, M.E.; Kabir, M.M.; Mridha, M.F.; Nishimura, S.; Shin, J. Deep learning and computer vision techniques for enhanced quality control in manufacturing processes. *IEEE Access* **2024**, *12*, 121449–121479. [CrossRef]
- 20. Junaid, A.; Siddiqi, M.U.R.; Mohammad, R.; Abbasi, M.U. In-process measurement in manufacturing processes. In *Functional Reverse Engineering of Machine Tool*, 1st ed.; Khan, W.A., Abbas, G., Rahman, K., Hussain, G., Edwin, C.A., Eds.; CRC Press: Boca Raton, FL, USA, 2019; pp. 105–134.
- 21. Li, N.; Wang, Z.; Zhao, R.; Yang, K.; Ouyang, R. YOLO-PDC: Algorithm for aluminum surface defect detection based on multiscale enhanced model of YOLOv7. *J. Real-Time Image Process.* **2025**, 22, 86. [CrossRef]
- 22. Ercetin, A.; Der, O.; Akkoyun, F.; Gowdru Chandrashekarappa, M.P.; Şener, R.; Çalışan, M.; Olgun, N.; Chate, G.; Bharath, K.N. Review of image processing methods for surface and tool condition assessments in machining. *J. Manuf. Mater. Process.* **2024**, *8*, 244. [CrossRef]
- 23. Tzampazaki, M.; Zografos, C.; Vrochidou, E.; Papakostas, G.A. Machine vision—Moving from industry 4.0 to industry 5.0. *Appl. Sci.* **2024**, *14*, 1471. [CrossRef]
- 24. Liu, W.; Li, F.; Jing, C.; Wan, Y.; Su, B.; Helali, M. Recognition and location of typical automotive parts based on the RGB-D camera. *Complex Intell. Syst.* **2021**, *7*, 1759–1765. [CrossRef]
- Cuesta, E.; Meana, V.; Álvarez, B.J.; Giganto, S.; Martínez-Pellitero, S. Metrology benchmarking of 3D scanning sensors using a ceramic GD&T-based artefact. Sensors 2022, 22, 8596. [CrossRef]
- 26. Ren, S.; He, K.; Girshick, R.; Sun, J. Faster R-CNN: Towards real-time object detection with region proposal networks. *IEEE Trans. Pattern Anal. Mach. Intell.* **2017**, 39, 1137–1149. [CrossRef]

27. Redmon, J.; Divvala, S.; Girshick, R.; Farhadi, A. You Only Look Once: Unified, Real-Time Object Detection. In Proceedings of the Conference on Computer Vision and Pattern Recognition, Las Vegas, NV, USA, 27–30 June 2016. [CrossRef]

- 28. Redmon, J.; Farhadi, A. YOLOv3: An incremental improvement. arXiv 2018, arXiv:1804.02767. [CrossRef]
- 29. Mery, D. Aluminum casting inspection using deep object detection methods and simulated ellipsoidal defects. *Mach. Vis. Appl.* **2021**, *32*, 72. [CrossRef]
- 30. Wang, C.-Y.; Bochkovskiy, A.; Liao, H.-Y.M. YOLOv7: Trainable Bag-Of-Freebies Sets new State-Of-The-Art for Real-Time Object Detectors. In Proceedings of the Conference on Computer Vision and Pattern Recognariation, Vancouver, BC, Canada, 17–24 June 2023. [CrossRef]
- 31. Tian, Y.; Ye, Q.; Doermann, D. Yolov12: Attention-centric real-time object detectors. arXiv 2025, arXiv:2502.12524. [CrossRef]
- 32. Hussain, M. Yolov1 to v8: Unveiling each variant-a comprehensive review of yolo. IEEE Access 2024, 12, 42816-42833. [CrossRef]
- 33. Parlak, İ.E.; Emel, E. Deep learning-based detection of aluminum casting defects and their types. *Eng. Appl. Artif. Intell.* **2023**, 118, 105636. [CrossRef]
- 34. Wang, P.; Jing, P. Deep learning-based methods for detecting defects in cast iron parts and surfaces. *IET Image Proc.* **2024**, *18*, 47–58. [CrossRef]
- 35. Xing, J.; Jia, M. A convolutional neural network-based method for workpiece surface defect detection. *Measurement* **2021**, 176, 109185. [CrossRef]
- 36. Duan, L.; Yang, K.; Ruan, L. Research on automatic recognition of casting defects based on deep learning. *IEEE Access* **2021**, 9, 12209–12216. [CrossRef]
- 37. Wang, L.; Song, C.; Wan, G.; Cui, S. A surface defect detection method for steel pipe based on improved YOLO. *Math. Biosci. Eng.* **2024**, *21*, 3016–3036. [CrossRef] [PubMed]
- 38. Terras, N.; Pereira, F.; Ramos Silva, A.; Santos, A.A.; Lopes, A.M.; Silva, A.F.d.; Cartal, L.A.; Apostolescu, T.C.; Badea, F.; Machado, J. Integration of deep learning vision systems in collaborative robotics for real-time applications. *Appl. Sci.* **2025**, 15, 1336. [CrossRef]
- 39. Sun, Z.; Caetano, E.; Pereira, S.; Moutinho, C. Employing histogram of oriented gradient to enhance concrete crack detection performance with classification algorithm and Bayesian optimization. *Eng. Fail. Anal.* **2023**, *150*, 107351. [CrossRef]
- 40. Wang, W.; Chen, Z.; Yuan, X. Simple low-light image enhancement based on Weber–Fechner law in logarithmic space. Signal Process. Image Commun. 2022, 106, 116742. [CrossRef]
- 41. Shen, H.; Wei, B.; Ma, Y. Unsupervised anomaly detection for manufacturing product images by significant feature space distance measurement. *Mech. Syst. Signal Process.* **2024**, 212, 111328. [CrossRef]
- 42. Mery, D. Aluminum casting inspection using deep learning: A method based on convolutional neural networks. *J. Nondestruct. Eval.* **2020**, *39*, 12. [CrossRef]
- 43. Nguyen, T.P.; Choi, S.; Park, S.-J.; Park, S.H.; Yoon, J. Inspecting method for defective casting products with convolutional neural network (CNN). *Int. J. Precis. Eng. Manuf. Green Technol.* **2021**, *8*, 583–594. [CrossRef]
- 44. Brenner, M.; Reyes, N.H.; Susnjak, T.; Barczak, A.L. RGB-D and thermal sensor fusion: A systematic literature review. *IEEE Access* **2023**, *11*, 82410–82442. [CrossRef]
- 45. Servi, M.; Mussi, E.; Profili, A.; Furferi, R.; Volpe, Y.; Governi, L.; Buonamici, F. Metrological characterization and comparison of D415, D455, L515 RealSense devices in the close range. *Sensors* **2021**, *21*, 7770. [CrossRef]
- 46. Andriyanov, N.; Khasanshin, I.; Utkin, D.; Gataullin, T.; Ignar, S.; Shumaev, V.; Soloviev, V. Intelligent system for estimation of the spatial position of apples based on YOLOv3 and Real Sense depth camera D415. *Symmetry* **2022**, *14*, 148. [CrossRef]
- 47. Van Crombrugge, I.; Sels, S.; Ribbens, B.; Steenackers, G.; Penne, R.; Vanlanduit, S. Accuracy assessment of joint angles estimated from 2D and 3D camera measurements. *Sensors* **2022**, 22, 1729. [CrossRef] [PubMed]
- 48. Xiang, Y.; Kim, W.; Chen, W.; Ji, J.; Choy, C.; Su, H.; Mottaghi, R.; Guibas, L.; Savarese, S. ObjectNet3D: A Large Scale Database for 3D Object Recognition. In Proceedings of the European Conference on Computer Vision, Amsterdam, The Netherlands, 8–16 October 2016. [CrossRef]
- 49. González Izard, S.; Sánchez Torres, R.; Alonso Plaza, Ó.; Juanes Méndez, J.A.; García-Peñalvo, F.J. Nextmed: Automatic imaging segmentation, 3D reconstruction, and 3D model visualization platform using augmented and virtual reality. *Sensors* 2020, 20, 2962. [CrossRef] [PubMed]
- 50. Rajamohan, G.; Sangeeth, P.; Nayak, P.K. On-machine measurement of geometrical deviations on a five-axis CNC machining centre. *Adv. Mater. Process. Technol.* **2022**, *8*, 269–281. [CrossRef]
- 51. Patel, D.R.; Kiran, M.B. Vision based prediction of surface roughness for end milling. *Mater. Today Proc.* **2021**, *44*, 792–796. [CrossRef]
- 52. Palani, S.; Natarajan, U. Prediction of surface roughness in CNC end milling by machine vision system using artificial neural network based on 2D Fourier transform. *Int. J. Adv. Manuf. Technol.* **2011**, 54, 1033–1042. [CrossRef]
- 53. Jiang, L.; Wang, Y.; Tang, Z.; Miao, Y.; Chen, S. Casting defect detection in X-ray images using convolutional neural networks and attention-guided data augmentation. *Measurement* **2021**, 170, 108736. [CrossRef]

54. Schlotterbeck, M.; Schulte, L.; Alkhaldi, W.; Krenkel, M.; Toeppe, E.; Tschechne, S.; Wojek, C. Automated defect detection for fast evaluation of real inline CT scans. *Nondestruct. Test. Eval.* **2020**, *35*, 266–275. [CrossRef]

- Yi-Cheng, L.; Syh-Shiuh, Y. Using Machine Vision to Develop an On-Machine Thread Measurement System for Computer Numerical Control Lathe Machines. In Proceedings of the International Multi-Conference of Engineers and Computer Scientists, Hong Kong, China, 13–15 March 2019.
- 56. Pérez, J.; León, J.; Castilla, Y.; Shahrabadi, S.; Anjos, V.; Adão, T.; López, M.Á.G.; Peres, E.; Magalhães, L.; Gonzalez, D.G. A cloud-based 3D real-time inspection platform for industry: A case-study focusing automotive cast iron parts. *Procedia Comput. Sci.* 2023, 219, 339–344. [CrossRef]
- 57. Zou, L.; Fang, H.; Li, Y.; Wu, S. Roughness estimation of high-precision surfaces from line blur functions of reflective images. *Measurement* **2021**, *182*, 109677. [CrossRef]
- 58. Huang, H.; Peng, X.; Wu, S.; Ou, W.; Hu, X.; Chen, L. An automotive body-in-white welding stud flexible and efficient recognition system. *IEEE Access* **2025**, *13*, 51938–51955. [CrossRef]
- 59. Khow, Z.J.; Tan, Y.F.; Karim, H.A.; Rashid, H.A.A. Improved YOLOv8 model for a comprehensive approach to object detection and distance estimation. *IEEE Access* **2024**, *12*, 63754–63767. [CrossRef]
- 60. Gasienica-Józkowy, J.; Cyganek, B.; Knapik, M.; Głogowski, S.; Przebinda, Ł. Deep learning-based monocular estimation of distance and height for edge devices. *Information* **2024**, *15*, 474. [CrossRef]
- 61. Huang, H.; Zhou, B.; Cao, S.; Song, T.; Xu, Z.; Jiang, Q. Aluminum reservoir welding surface defect detection method based on three-dimensional vision. *Sensors* **2025**, *25*, 664. [CrossRef]
- 62. Myśliwiec, P.; Kubit, A.; Szawara, P. Optimization of 2024-T3 aluminum alloy friction stir welding using random forest, XGBoost, and MLP machine learning techniques. *Materials* **2024**, 17, 1452. [CrossRef] [PubMed]
- 63. Chen, Y.; Wu, Y. Detection of welding defects tracked by YOLOv4 algorithm. Appl. Sci. 2025, 15, 2026. [CrossRef]
- 64. Shao, D.; Liu, Y.; Liu, G.; Wang, N.; Chen, P.; Yu, J.; Liang, G. YOLOv7scb: A small-target object detection method for fire smoke inspection. *Fire* **2025**, *8*, 62. [CrossRef]

Disclaimer/Publisher's Note: The statements, opinions and data contained in all publications are solely those of the individual author(s) and contributor(s) and not of MDPI and/or the editor(s). MDPI and/or the editor(s) disclaim responsibility for any injury to people or property resulting from any ideas, methods, instructions or products referred to in the content.